Wavefront Calculations

O. Chubar

European Synchrotron Radiation Facility, BP 220, F-38043 Grenoble Cedex, France

ABSTRACT

Methods and results of synchrotron radiation wavefront calculations in the framework of scalar diffraction theory are discussed. First, wavefront peculiarities of undulator and bending magnet radiation are considered in single-electron approximation, in comparison with a point source. The consideration includes the effects related to finite electron beam emittance in storage ring sources. Finally, examples of SASE wavefront computation are presented.

Keywords: synchrotron radiation, wave optics, wavefront, focusing.

1. INTRODUCTION

The questions related to the synchrotron radiation (SR) wavefront propagation were considered in a number of papers at different levels of detail. The SR focusing was treated in the pioneering paper [1], where the analytical methods of Gaussian optics were applied to estimate spatial resolution at electron beam imaging with synchrotron light. A general approach to treatment of SR propagation based on Wigner distributions was suggested in [2]. A particular case of focusing the bending magnet SR was considered in [3] taking into account the effect of truncation of the radiation by aperture. A method of computation of the focused bending magnet radiation treating the SR emission and diffraction on the lens aperture in the frame of the scalar diffraction theory was suggested in [4]. The wave-optical features of the bending magnet SR were discussed in [5,6]. The phase peculiarities and focusing efficiencies of different types of SR were considered in [7]. A few wave-optics computer codes allowing simulation of the SR wavefront propagation through beamline components have appeared recently [8,9].

In the wavefront calculations described in this paper, the frequency-domain electric field of the single-electron SR and the self-amplified spontaneous emission (SASE) is treated. A very special attention is paid to the phase of the electric field as a function of transverse position, which is of particular importance for the wavefront propagation through optical components and free space. In each of the considered cases of emission, the electric field is characterized by a special phase correction, which, after being added to the phase of the electric field, gives the phase of a point source [7]. To estimate the effect of the phase correction, we consider two options of a simple 1:1 imaging scheme. In one option, the radiation is focused only by an aberration-free optical component simulated by a thin lens; in the other option, a numerically computed phase correction is applied to the wavefront just in front of the lens. Spectral flux per unit surface (called intensity throughout the rest of this paper) of the radiation propagated to the image plane is compared for these two options.

The initial electric field is computed using high accuracy near-field methods. This computation preserves all the phase terms that are necessary for further propagation of the radiation through optical components and drift spaces in a beamline [9,10]. The propagation is simulated using the principles of Fourier optics.

The next section shortly describes the methods used for the single-electron SR wavefront computation, and recalls the basic principles of the Scalar Diffraction theory and Fourier optics, as applied to the SR. Section 3 presents the computation examples and considers the wave-optical features of the single-electron SR and SASE.

2. SR EMISSION AND PROPAGATION IN THE FREQUENCY DOMAIN

2.1. Single-Electron Emission

A very popular approach to compute the electric field of radiation emitted by one electron treats separately the terms depending on the electron acceleration and its velocity [11]. This section describes another frequency-domain approach, which can be advantageous for the near-field calculations. This approach is based on the scalar and vector retarded potentials [11,12] (Gaussian system):

$$\vec{A} = e \int_{-\infty}^{+\infty} \frac{\vec{\beta}}{R} \cdot \delta(\tau - t + R/c) d\tau \, ; \quad \varphi = e \int_{-\infty}^{+\infty} \frac{1}{R} \cdot \delta(\tau - t + R/c) d\tau \, , \tag{1}$$

where $\delta = \delta(x)$ is delta-function, $\vec{\beta} = \vec{v}(\tau)/c$ is instant relative velocity of electron, $R = R(\tau)$ is distance from the electron to the observation point, c is the speed of light, e is the charge of electron. After applying the representation of the delta-function by a Fourier integral, one obtains:

$$\vec{A} = \frac{e}{2\pi} \int_{-\infty}^{+\infty} \exp(-i\omega t) d\omega \int_{-\infty}^{+\infty} \frac{\vec{\beta}}{R} \cdot \exp[i\omega(\tau + R/c)] d\tau ; \quad \varphi = \frac{e}{2\pi} \int_{-\infty}^{+\infty} \exp(-i\omega t) d\omega \int_{-\infty}^{+\infty} \frac{1}{R} \cdot \exp[i\omega(\tau + R/c)] d\tau , \quad (2)$$

where the frequency ω was introduced. Then, assuming convergence of all integrals, the time-domain electric field is:

$$\vec{E} = -\frac{1}{c}\frac{\partial \vec{A}}{\partial t} - \nabla\varphi = \frac{ie}{2\pi c} \int_{-\infty}^{+\infty} \omega \cdot \exp(-i\omega t) d\omega \int_{-\infty}^{+\infty} \frac{1}{R}\left[\vec{\beta} - \vec{n} \cdot \left(1 + \frac{ic}{\omega R}\right)\right] \cdot \exp[i\omega(\tau + R/c)] d\tau , \quad (3)$$

where $\vec{n} = \vec{R}(\tau)/R(\tau)$ is unit vector directed from instant electron position to the observation point. From eq. (3), one obtains the frequency-domain electric field:

$$\vec{E}_\omega = \frac{ie\omega}{c} \int_{-\infty}^{+\infty} \frac{1}{R}\left[\vec{\beta} - \vec{n}\left(1 + \frac{ic}{\omega R}\right)\right] \cdot \exp[i\omega(\tau + R/c)] d\tau , \quad (4)$$

where, following [12], the notation $\vec{E}_\omega \equiv \int_{-\infty}^{+\infty} \vec{E} \exp(i\omega t) dt$ is used.

One can show the equivalence of the eq. (4) and the representation through the acceleration and velocity terms [11], using the integration by parts and assuming non-zero frequency. Similarly to eqs. (3) and (4), the expressions for the magnetic field $\vec{H} = \nabla \times \vec{A}$ can be derived. In many cases, however, the approximation $\vec{H} = \bar{\vec{n}} \times \vec{E}$ (where $\bar{\vec{n}}$ is averaged value of $\vec{n}$) is acceptable, so one can consider only the electric field (3), (4).

For practical calculations of emission by relativistic electrons in accelerators, one can apply the following expansion of the phase in eq. (4), which assumes small observation angles and preserves the variation of the observation distance R with the electron position:

$$\omega(\tau + R/c) \approx (2\pi/\lambda) \, y^* + \Phi(s),$$

$$\Phi(s) = \frac{\pi}{\lambda}\left[s\gamma^{-2} + \int_0^s |\vec{\beta}_\perp|^2 \, d\tilde{s} \;+\; \frac{(x^*-x)^2 + (z^*-z)^2}{y^*-s}\right], \quad (5)$$

where the trajectory length $s = \tau \, |\vec{\beta}| \, c$ is used as an integration variable, $x=x(s)$, $z=z(s)$ are instant transverse coordinates of the electron, $\vec{\beta}_\perp = \vec{\beta}_\perp(s)$ is transverse component of the relative velocity vector $\vec{\beta}(s)$; x^* and z^* are horizontal and vertical coordinates of the observation point, y^* is its longitudinal coordinate; $\gamma(\gg 1)$ is the reduced electron energy, λ the radiation wavelength.

For the efficiency of computation, one can apply the following simplest asymptotic expansion of the integral (4) for those pieces of trajectory, where the exponent phase changes strongly and monotonously:

$$\int_{-\infty}^{+\infty} F \exp(i\Phi) ds = \int_{s_1}^{s_2} F \exp(i\Phi) ds + \int_{-\infty}^{s_1} F \exp(i\Phi) ds + \int_{s_2}^{+\infty} F \exp(i\Phi) ds ,$$

$$\int_{-\infty}^{s_1} F \exp(i\Phi) ds + \int_{s_2}^{+\infty} F \exp(i\Phi) ds \approx \left[\left(\frac{F}{i\Phi'} + \frac{F'\Phi' - F\Phi''}{\Phi'^3} + ...\right) \exp(i\Phi)\right]_{s_2}^{s_1} . \quad (6)$$

The convergence (up to given precision level) of the expansion (6) for a particular choice of the separating points s_1, s_2 can be checked practically at the computation.

The method based on eqs. (4), (5) allows to efficiently compute many cases of spontaneous emission for the observation either in the near or far field. It was implemented in the SRW computer code [9]. This method is also convenient for further analytical calculations, like integration with a function describing particle distribution in phase space, in order to simulate coherent multi-electron emission, or the treatment of incoherent emission by a "thick" electron beam [10].

Besides the single-electron wavefront calculations, this paper considers a few examples with the SASE wavefronts. At these calculations, a numerical solution of paraxial free-electron laser (FEL) equations in approximation of slowly varying amplitude of radiation field, was used to compute the frequency domain electric field at an exit of SASE undulator. For an overview of the FEL theories and methods of calculations one can refer to [13,14].

2.2. Helmholtz-Kirchhoff Theorem and Fourier Optics

In the Scalar Diffraction theory [15], the propagation of radiation in free space is described by the Helmholtz-Kirchhoff theorem, which gives the value of a function U at some point P^* if its values (and the values of its normal derivative) on the surrounding surface Σ are known:

$$U(P^*) = \frac{1}{4\pi} \iint_{\Sigma} \left[U \frac{\partial}{\partial \vec{\ell}} \left[\frac{\exp(ikS)}{S} \right] - \frac{\exp(ikS)}{S} \frac{\partial U}{\partial \vec{\ell}} \right] d\Sigma, \qquad (7)$$

where $k = \omega/c$ is wave number, S is the distance between a point P' on the surface Σ and the observation point P^*. The application of eq. (7), and the Kirchhoff's boundary conditions [15], to the transverse components of the single-electron electric field (4) gives, at $\lambda \ll R$, $\lambda \ll S$:

$$\vec{E}_{\omega\perp}(P^*) = \frac{k^2 e}{4\pi} \int_{-\infty}^{+\infty} d\tau \iint_A \frac{\vec{\beta}_\perp - \vec{n}_\perp}{RS} \exp[ik(c\tau + R + S)] \cdot [(\vec{\ell} \cdot \vec{n}) + (\vec{\ell} \cdot \vec{n}_{p'p^*})] d\Sigma, \qquad (8)$$

where $\vec{n}_{p'p^*}$ is unit vector from the point P' to the observation point P^*, $\vec{\ell}$ is unit vector normal to the surface Σ and directed inside the volume. The inner integration in eq. (8) is done within an aperture A (or a part of the surface Σ where the incident electric field is not zero). Eq. (8) can be treated as a sum of contributions from point sources located on the electron's trajectory, with varying phases and amplitudes.

At small angles: $(\vec{\ell} \cdot \vec{n}) + (\vec{\ell} \cdot \vec{n}_{p'p^*}) \approx 2$, and eq. (8) gives the well-known Huygens-Fresnel principle:

$$\vec{E}_{\omega\perp}(P^*) = -ik(2\pi)^{-1} \iint_A \vec{E}_{\omega\perp}(P') \cdot S^{-1} \exp(ikS) \, d\Sigma, \qquad (9)$$

where $\vec{E}_{\omega\perp}(P')$ is given by eq. (4). Due to small emission angles and typically large observation distances in storage rings and FELs, the approximation (9) is well suited for many cases of spontaneous emission and SASE.

If the integration surface in eq. (9) is a plane, then for the observation points P^* located on another plane parallel to A, eq. (9) is a convolution-type integral, which can be computed quickly using the fast Fourier transforms and the convolution theorem. This gives a CPU-efficient method of wavefront propagation through drift spaces.

In the approximation of Fourier optics, the propagation of the transverse electric field through simple optical components (lenses, apertures, etc.) is described by multiplication of the electric field by a complex transmission function. For more complicated components, one can apply analytical methods (for example, the stationary phase method) to derive the transformation of the electric field at propagation from a plane before the optical component to a plane immediately after it.
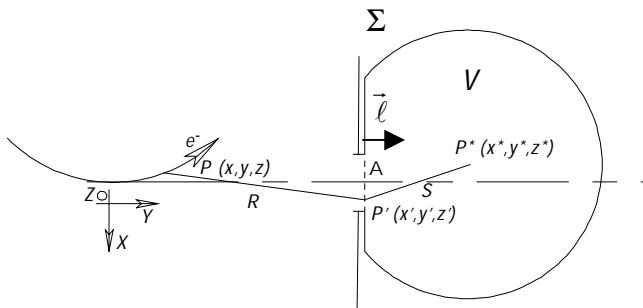

Figure 1. Illustration for the Helmholtz-Kirchhoff theorem applied to synchrotron radiation.

2.3. Phase Correction

Let $E_{in}(x,z)$ be a scalar complex function of horizontal and vertical coordinates describing one polarization component (linear or circular) of the frequency domain electric field of radiation at wavelength λ in a transverse plane after which an optical component(s) can be placed. The distance from the source (for example, from the middle of undulator) to that plane is approximately equal to R. We would like to apply a phase correction $\Phi_{cor}(x,z)$, i.e., a transformation

$$T(x,z) = \exp[i\Phi_{cor}(x,z)], \tag{10}$$

to the electric field $E_{in}(x,z)$, so that its phase becomes identical to that of a point source:

$$E_{out}(x,z) = T(x,z)E_{in}(x,z) = A(x,z)\exp[i\pi(x^2+z^2)/(\lambda R)], \tag{11}$$

where $A(x,z)$ is the amplitude of the electric field (that we don't intend to modify by the transformation T). Then immediately from eqs. (10) and (11) we obtain:

$$\Phi_{cor}(x,z) = \arg[\exp[i\pi(x^2+z^2)/(\lambda R) + i\Phi_0]/E_{in}(x,z)], \tag{12}$$

where, without loss of generality, the principal value of the argument function is assumed; Φ_0 is arbitrary constant. Eqs. (11), (12) imply small observation angles. It is also assumed that the amplitude of the electric field is never equal exactly to zero within the range where the transformation $T(x,z)$ is applied.

We have chosen to transform the phase of the SR electric field to that of a point source, because after such transformation, one can safely apply standard optical components dedicated to point sources for further propagation of the radiation in a beamline. One can show that the use of the phase correction (12) with a focusing optical component dedicated to a point source results in the highest peak intensity in the image plane, which is possible to obtain without modifying the amplitude of the electric field at the optical component. However, the correction (12) may not guarantee the smallest possible spot size in the image plane.

It is important to note that the phase correction (12), which is derived for only one polarization component of electric field, does not guarantee a proper transformation for another polarization component. In many practical cases, however, only one SR polarization component is dominating (linear horizontal in planar undulators, circular right or left in helical undulators, etc.), so this obstacle may not pose a big problem.

This paper does not treat the question of possible practical implementation of the phase corrections. One could mention, however, that for normal-incidence transmission optics, the phase shift is proportional to the thickness of the material of the optical component. Therefore, a straightforward implementation of the phase correction derived using eq. (12) could be a kind of special zone plate.

3. EXAMPLES OF CALCULATION

3.1. Single-Electron Wavefronts

3.1.1. Undulator Radiation

Let us consider the radiation emitted by a filament electron beam at an energy of 6 GeV, current 0.2 A in a planar undulator with 38 periods of 42 mm, peak magnetic field of 0.56 T (U42 undulator at the ESRF). The emitted radiation is initially considered at a distance of 30 m from the undulator, where a focusing component should be placed. The goal is to obtain the highest peak intensity and the smallest spot size at 30 m from the optical component (1:1 imaging).

As the first example related to the focusing of undulator radiation (UR), we computed intensity distribution of the UR focused by a thin lens, for several photon energies close to the on-axis peak value of the fundamental harmonic. The computation results are presented in fig. 2. As one can see, the maximum peak intensity is obtained at the photon energy of 2.36 keV, which is slightly lower than the on-axis peak value of the fundamental. For this photon energy, the intensity distribution at the lens represents a small ring, rather than a cone with a maximum on axis (left graph in fig. 2). This feature of undulator radiation was discussed in [1].
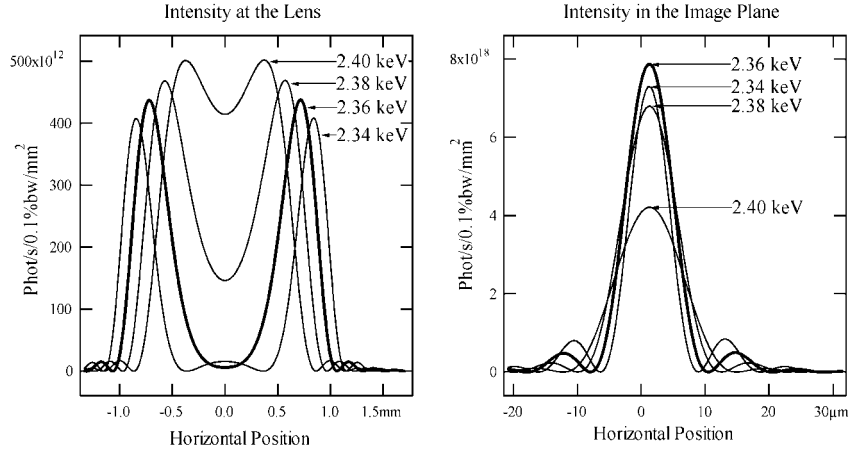
Figure 2. Intensity distribution of UR (horizontal cuts by the median plane) for four photon energies close to the on-axis peak value of the fundamental harmonic, at the position of the lens 30 m from the undulator (left) and in the plane of 1:1 imaging (right). The lens aperture is 3.4 mm x 3.4 mm.
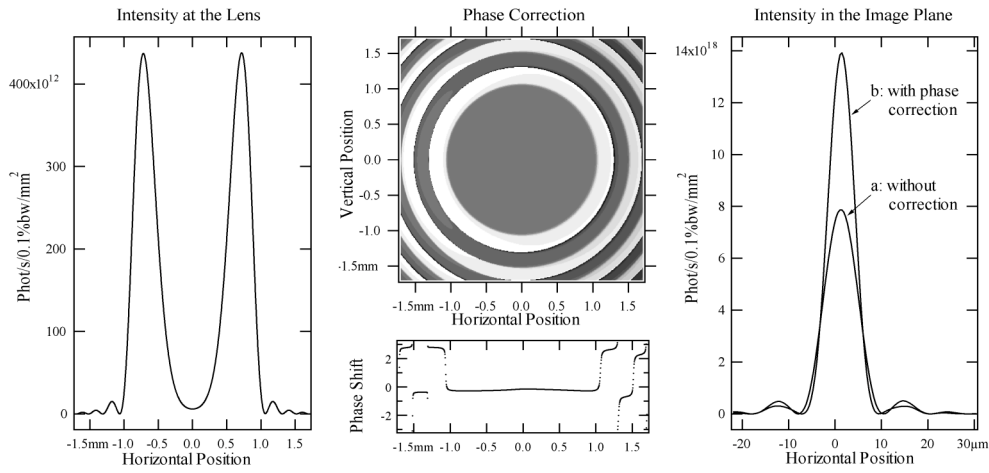

Figure 3. Left: intensity distribution (horizontal cut by the median plane) of horizontally polarized radiation emitted at the fundamental harmonic of a planar undulator at 2.36 keV photon energy (which is slightly smaller than the on-axis peak value of the fundamental, and gives the highest peak intensity in the spot if focused by a perfect lens), at the longitudinal position of the lens. Middle: phase correction computed numerically. Right: intensity distributions in the image plane (horizontal cuts) for the UR focused without any phase correction (a), and with the phase correction applied at the longitudinal position of the lens (b).

The phase correction was then computed for the UR at a photon energy of 2.36 keV, which gave the highest peak intensity in the focused spot, and the focusing of this radiation with the phase correction applied at the longitudinal position of the lens was simulated. The intensity distribution at the lens, the phase correction according to eq. (12), and the intensity in the plane of 1:1 imaging of the UR focused with and without the phase correction are shown in fig. 3. As one can see, the use of the phase correction allows the peak intensity in the focused spot to increase further (by a factor of ~ 1.8 in the example considered).

The phase correction for odd harmonics of radiation from a planar undulator mainly consists in changing the phase of the rings surrounding the central cone (or the main central ring), consecutively by π. Here we consider the rings immediately following the central cone (or the central ring) and belonging to the same harmonic. If the aperture of an optical component can only accept a part of the UR central cone, there is no sense in applying any phase correction.
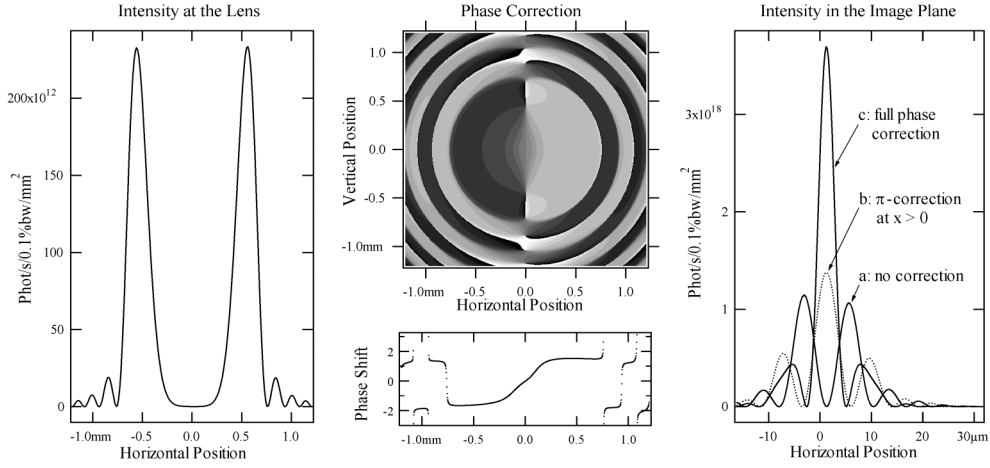
Figure 4. Left: intensity distribution (horizontal cut by the median plane) of horizontally polarized radiation emitted at the second harmonic of a planar undulator (4.775 keV photon energy) at the longitudinal position of the lens. Middle: phase correction computed numerically. Right: intensity distributions in the image plane (horizontal cuts) for the UR focused without any phase correction (a), with half-wave correction at $x > 0$ (b), and with the full phase correction applied at the longitudinal position of the lens (c). The aperture is 2.4 mm x 2.4 mm.
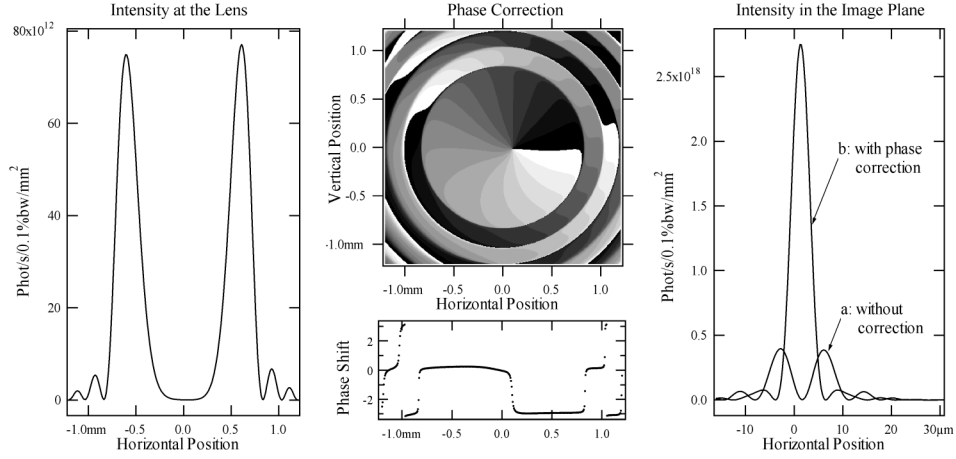

Figure 5. Left: intensity distribution (horizontal cut by the median plane) of circularly polarized radiation emitted at the second harmonic of a helical undulator (4.20 keV photon energy) at the longitudinal position of the lens. Middle: phase correction computed numerically. Right: intensity distributions in the image plane (horizontal cuts) for the UR focused without any phase correction (a), and with the phase correction applied at the longitudinal position of the lens (b). The aperture is 2.4 mm x 2.4 mm.

In the next example we consider the second harmonic of the UR from the same undulator at the same observation conditions. Even harmonics of radiation from a planar undulator are well known to be suppressed in the on-axis direction, however, a considerable photon flux is emitted into the rings with diameters and widths dependent on the photon energy value. Fig. 4 presents computation results of the UR intensity at 4.775 keV photon energy (second harmonic) at the lens, the phase correction, and intensity distribution in the plane of 1:1 imaging, if focused with and without the phase correction.

The phase correction for even harmonics of radiation from a planar undulator consists in the same type of correction as for odd harmonics and, in addition to this, in changing the phase by π at $x > 0$ compared to $x < 0$. The latter is a consequence of anti-symmetry of the horizontal electric field over the horizontal position at even harmonics. We note that a similar situation takes place for the vertical polarization component of conventional bending magnet radiation, which is anti-symmetrical

over the vertical position. Due to this anti-symmetry, there is no peak intensity in the centre of the focused spot in these cases. As we see from fig. 4, the use of a simple half-wave shift at $x > 0$ (or at $x < 0$) removes the anti-symmetry of the electric field and thus brings the maximum intensity to the center of the focused spot. However, the use of the full phase correction shown in the middle of fig. 4, results in considerably higher peak intensity in the spot (right graph in fig. 4).

As the last illustration of phase corrections for UR, we consider the case of a helical undulator. The phase correction for a fundamental harmonic of radiation from a helical undulator looks identical to that of odd harmonics of a planar undulator (fig. 3), however, the situation with the other harmonics is different. The harmonics higher than one are not emitted in the on-axis direction in helical undulators. Due to this obstacle, very often they are not even considered for practical use. Yet there is a lot of circularly polarized radiation that is emitted into rings at these harmonics. This radiation could be well used in experiments.

To illustrate, we take the following parameters: filament electron beam at an energy of 6 GeV, current 0.2 A in a helical undulator with 28 periods of 52 mm, peak horizontal and vertical magnetic fields of 0.3 T. The radiation at 4.20 keV photon energy (second harmonic) is initially considered at a distance of 30 m from the undulator, where a focusing optical component should be placed. As in previous examples, the goal is to obtain the highest peak intensity and the smallest spot size at 30 m from the optical component. Fig. 5 shows the results of simulations.

The phase correction for higher harmonics of a helical undulator consists in the same type of correction as for odd harmonics of a planar undulator (see fig. 3) and, in addition to this, in the linear change of the phase with an azimuth angle (fig. 5). The effect of the phase correction is greater in this case compared to other UR cases considered (the peak intensity increased by a factor of 8 in our example).

The phase correction for different types of undulator radiation at harmonic number n (central cone and adjacent rings) can be approximated as follows:

$$\Phi_{cor\,UR} \approx \pi\eta(\theta - \theta_{nN-l_0}) + \pi g(n, \theta_x, \theta_z) + \pi\, \mathrm{sgn}(\theta_{nN-l_0} - \theta)\sum_{k=0}^{k_{max}} \eta(\theta - \theta_{2k})\eta(\theta_{2k+1} - \theta);$$

$$\theta_l = (2\lambda/L)^{1/2}\left| l + l_0 - \lambda_1 N/\lambda \right|^{1/2}\eta(l); \qquad l_0 = \left[\lambda_1 N/\lambda\right] + 1,$$

(13)

where η is the step function ($\eta = 0$ if $x<0$ and $\eta = 1$ if $x\geq0$), sgn is the sign function (-1 if $x<0$ and 1 if $x\geq0$); θ_x, θ_z are horizontal and vertical observation angles ($|\theta_x|<<1, |\theta_z|<<1$), $\theta \equiv (\theta_x^2 + \theta_z^2)^{1/2}$; N is the number of periods, λ_1 the wavelength of the fundamental harmonic on axis. k_{max} is obtained from the relation: $\theta_{2k_{max}} \leq \theta_{max}$, with θ_{max} giving the angular aperture. Square braces in the expression for l_0 mean an integer part of a number (in other parts of this paper, the square braces do not have such meaning). Function $g(n, \theta_x, \theta_z)$ is specific to the type of undulator:

for planar undulator:
$$g(n, \theta_x, \theta_z) \approx \begin{cases} 0, & n = 1,3,... \\ \eta(\theta_x), & n = 2,4,... \end{cases}$$

for helical undulator:
$$g(n, \theta_x, \theta_z) \approx (-1)^p (n-1)\left[\arccos\left[[2\eta(\theta_z) - 1]\theta_x/\theta\right]/\pi - \eta(\theta_z) + 1\right],$$

(14)

where arccos and step functions are used to express the azimuth angle via θ_x, θ_z; $p = 0$ or 1 depending on the UR polarization (right or left). The approximation (14) is valid at $\lambda > \lambda_1/n$, with improved accuracy for larger wavelengths.

The eqs. (13), (14) accord with the phase corrections calculated numerically using the near-field SR computation method (figs. 3 - 5). We note that these corrections do not depend on the observation distance. The reason is that, regarding the above consideration, we limited ourselves to relatively small angles comparable with the UR central cone or small rings of emission at given harmonics. The dependence on the observation distance may appear as one considers larger observation angles. In such cases eqs. (13), (14) may not be valid. However, one can still treat the problem numerically, using the eq. (12) or a more sophisticated algorithm. We emphasize the necessity of near-field SR computation for such purposes. The near-field effects in the off-axis undulator radiation were discussed in [16].

For efficient practical use of the phase corrections for undulator radiation in storage rings, the apparent angular divergence of the electron beam should be smaller than the angular width of the largest UR ring accepted by the aperture of the optical component, and the transverse size of the electron beam should be at least smaller than the spot size of the focused UR central cone (assuming 1:1 imaging). As a very rough estimation,

$$(\Delta'^2_{x,z} + \Delta^2_{x,z}/R^2)^{1/2} \ll (\lambda/L)^{1/2}; \quad \Delta_{x,z} \ll (\lambda L)^{1/2}, \tag{15}$$

where $\Delta'_{x,z}, \Delta_{x,z}$ mean horizontal (vertical) angular divergence and transverse size of the electron beam respectively, L is the lens of the undulator. Note that it formally follows from eq. (16) that the source should be diffraction-limited: $\Delta_{x,z}\Delta'_{x,z} \ll \lambda$. For even harmonics of a planar undulator, or harmonics $n > 1$ of a helical undulator, one can have some gain even if the first relation in (15) is not satisfied.

3.1.2. Bending Magnet SR

Consider a case of bending magnet radiation at the following emission and observation conditions: electron beam energy of 2.5 GeV, current 0.5 A; constant field in bending magnet 1.56 T; photon energy 40 eV, horizontal angular aperture 6 mr, vertical aperture 4 mr (~natural opening angle of the bending magnet SR); distance from tangential source point to optical component 5 m.

Surface plots of intensity distributions and phase corrections for the horizontal SR polarization component computed numerically at these conditions are shown in fig. 6. The branch of the phase function equal to zero at zero transverse positions was taken in eq. (12). The phase correction for the vertical component of the electric field differs from the correction for the horizontal component by a π- flip at zero vertical position. This is a consequence of anti-symmetry of the vertical electric field with respect to the plane of the electron beam orbit.

Computation results of intensity in the plane of 1:1 imaging are presented in fig. 7. Due to the phase differences of the bending magnet SR from that of a point source, there is an aberration in the focused spot, if the focusing is performed by an optical component dedicated to a point source (left plots in fig. 7). For single electron radiation, this aberration appears when the horizontal aperture is comparable with the natural opening angle of the bending magnet SR, and it becomes larger as the horizontal aperture further increases. These results accord with the simulations performed earlier by another computation method that gives the intensity distribution of the focused SR in the image plane without the need to compute the SR wavefront at the position of the lens [4], and the results presented in [5].

Middle and right plots in fig. 7 show the effect of the phase corrections for the horizontal component of the electric field. The phase correction removes large secondary maximums of intensity distribution of the focused SR, reduces the RMS spot size and increases the peak intensity (upper right plot in fig. 7). The peak intensity is increased by more than a factor of 2 in the example considered. The effect becomes more valuable with the increase of the horizontal aperture.
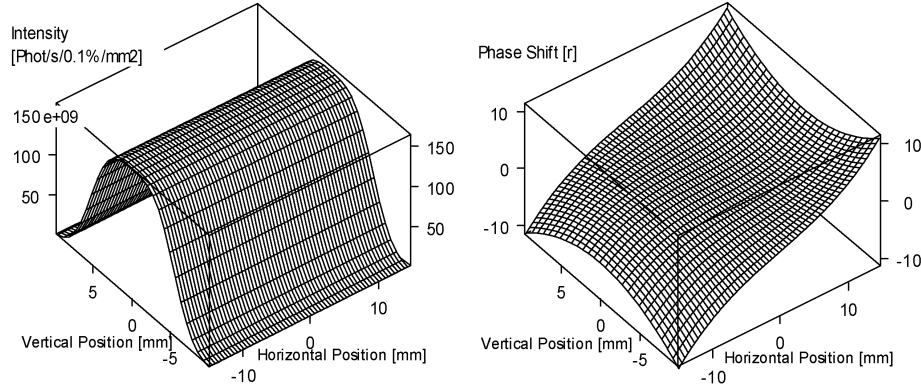

Figure 6. Left: intensity distribution of the bending magnet radiation (horizontal polarization component) in transverse plane at 5 m from the tangential "source point". Right: phase correction.
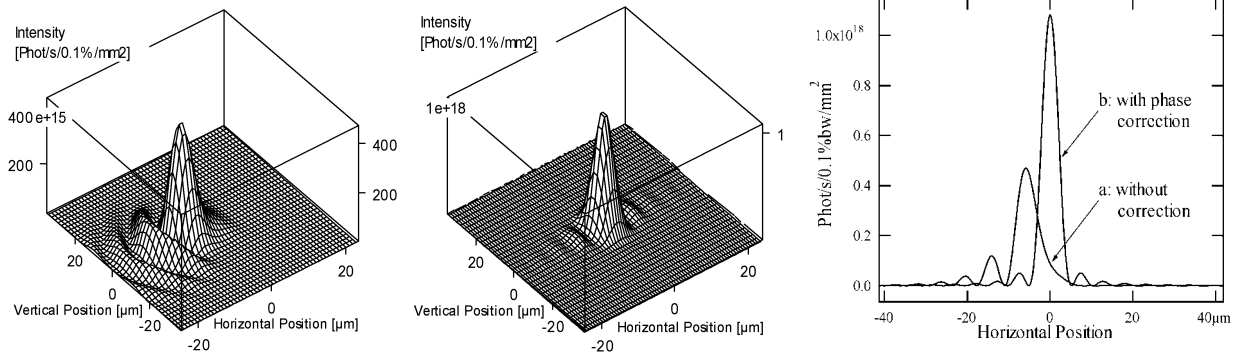
Figure 7. Intensity distributions of the focused bending magnet SR (horizontal polarization component). Left: focusing by aberration-free "thin lens", without any phase correction. Middle: focusing with the phase correction applied at the longitudinal position of the lens (the correction is different for horizontal and vertical polarization components). Right: horizontal (for horizontal polarization component) and vertical (for vertical polarization component) cuts of intensity in the spot for the focusing without (a) and with (b) the phase correction.

The phase correction for the conventional bending magnet SR is described analytically by [5-7]:

$$\Phi_{cor\,BM\,hor} \approx -(\pi/\lambda)\rho\theta_x(\gamma^{-2} + \theta_x^2/3 + \theta_z^2),$$

$$\Phi_{cor\,BM\,vert} = \Phi_{cor\,BM\,hor} + \pi\eta(\theta_z),$$

(16)

where ρ is bending radius, θ_x and θ_z observation angles. Eqs. (16) imply small observation angles ($|\theta_x| << 1, |\theta_z| << 1$) and a small longitudinal size of the emission region compared to the observation distance ($\min[(\lambda\rho^2)^{1/3}, \lambda\gamma^2] << R$). Both requirements are well satisfied in storage rings. Note that eqs. (16) do not depend on the observation distance, i.e. the phase difference between the bending magnet SR and a point source is not a consequence of near-field effects: it can take place at large distances from the bending magnet, if the horizontal aperture is large enough.

For the effects described to take place with a finite-emittance electron beam, the apparent angular divergence of the electron beam should be considerably smaller than the natural opening angle of the bending magnet SR, and the transverse size of the electron beam should be smaller than the spot size of the focused single electron SR (assuming 1:1 imaging):

$$(\Delta_{x,z}'^2 + \Delta_{x,z}^2/R^2)^{1/2} << \min[\lambda\gamma^2/|\rho|, (\lambda/|\rho|)^{1/3}]; \quad \Delta_{x,z} << \max[|\rho|\gamma^{-2}, (\lambda^2|\rho|)^{1/3}].$$

(17)

In practice, the first relation in (17) is met in storage ring SR sources up to very hard X-rays; however, the second one can be satisfied for typical values of the horizontal size of the electron beam only in infrared range.

3.2. SASE Wavefronts

This section describes an example of SASE wavefront calculations performed for a set parameters close to those of the X-FEL [17]: electron beam energy of 25 GeV, normalized electron beam emittance of ~1 π mm×mr, horizontal and vertical RMS electron beam size of 20.3 μm; planar undulator with the period length of 48.5 mm, deflection parameter of ~4.2, fundamental harmonic wavelength of ~1 Å.

The SASE computation was done using the 3D code GENESIS [18] adapted and interfaced to the SRW code [9]. The wavefront at the beginning of the undulator was assumed Gaussian with the initial peak power predicted by one-dimensional theory [19]. To reduce the CPU time, the effect of the FODO lattice was simulated by enlarging the natural focusing of the undulator beyond the normal values, as suggested in [20]. After the exit of the undulator, the wavefront was further propagated in free space and analyzed using the Fourier optics methods implemented in the SRW code.

Fig. 8 shows the computed peak radiation power vs. longitudinal position in the undulator (upper graph), and the horizontal profiles of the radiation intensity at the exit of the undulator, for several different numbers of periods: 1500, 2500, 3500 and 4500 (middle graphs). For each of these four cases, the wavefront was propagated after the exit of undulator by 500 m in

free space. The corresponding intensity profiles are shown in lower graphs in fig. 8. As one can see from fig. 8, the wavefront preserves the Gaussian shape in the region where the saturation still is not reached. After the saturation is reached (at ~100 m in the example considered), the wavefront starts to differ from that of a Gaussian beam. Due to oscillatory behavior of the power gain after the saturation, the intensity profiles of the propagated wavefronts possess the fringes (lower-right graphs in fig. 8), which can be interpreted as resulting from the interference between radiations from those intervals of the electron beam path, where the emitted power is higher.

To further characterize the features of the computed wavefronts, we consider the simplest imaging scheme with a lens located at 500 m from the exit of undulator, and the image plane at a distance of 500 m from the lens. For this scheme, we compute phase correction at the position of the lens, and then the intensity distributions in the image plane for the wavefront propagated with and without the phase correction. The results of this computation for three different numbers of periods in the undulator (1500, 2500 and 3500) are shown in fig. 9. The phase of non-saturated wavefront after 1500-period undulator (fig. 9-a) was found to be very close to that of a virtual point source located ~16 m before the exit of the undulator, so that no special correction seems necessary for the efficient focusing of this wavefront. The computed phase corrections for the two other cases (2500 and 3500 period undulators, saturated wavefronts) are shown in the middle figs. 9-b,c. One can see that these phase corrections depend on the length of the electron beam path and the beam dynamics after the saturation.

One can expect that in practice, the phase of SASE wavefront may differ from that of a point source even before the saturation because of the stochastic "origin" of the initial non-amplified weavefront, and such possible effects like "competition of modes", that were not taken into account at this computation.
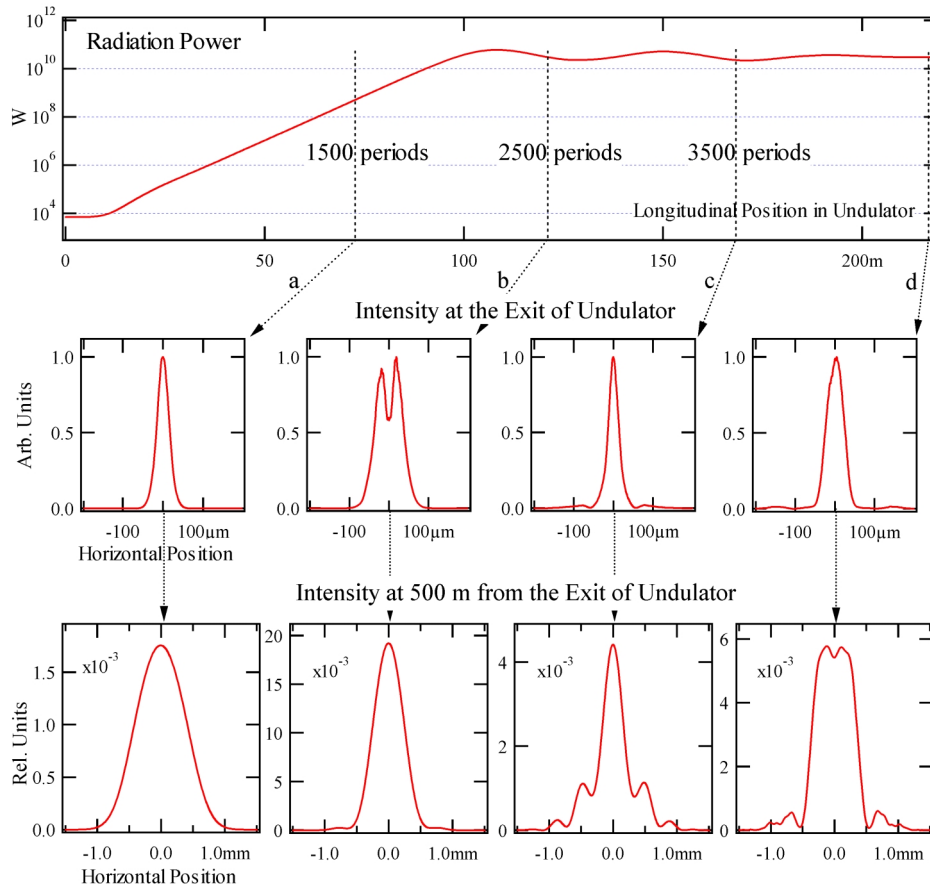

Figure 8. Computed peak power (upper graph) and horizontal intensity profiles of SASE wavefronts at the fundamental wavelength (~1 A) for different numbers of periods in the undulator, at the exit of undulator (middle graphs) and at a distance of 500 m from the exit of undulator (lower graphs).

Intensity at the Lens
(500 m from the Undulator)

Wavefront Radius
and Phase Correction
(500 m from the Undulator)

Intensity in the Image Plane
(500 m from the Lens)

a) 1500 periods (72.75 m, non-saturated)

$R_{wf} = 516$ m

$|\Delta\Phi| < 0.2$

1.0

0.5

0.0

-1.0   0.0   1.0mm
Horizontal Position

1000

500

0

-100 -50   0   50 100μm
Horizontal Position

b) 2500 periods (121.25 m, saturated)

$R_{wf} \sim 527$ m

1.0

0.5

0.0

-1.0   0.0   1.0mm
Horizontal Position

1.0
Vertical Position
0.5
0.0
-0.5
-1.0mm

-1.0 -0.5   0.0   0.5   1.0mm
Horizontal Position

Phase Shift
2.5

0.0

-1.0 -0.5   0.0   0.5   1.0mm

200

100

0

with phase
correction

without
correction

-100 -50   0   50 100μm
Horizontal Position

c) 3500 periods (169.75 m, saturated)

$R_{wf} \sim 545$ m

1.0

0.5

0.0

-1.0   0.0   1.0mm
Horizontal Position

1.0mm
Vertical Position
0.5
0.0
-0.5
-1.0

-1.0mm -0.5 0.0 0.5   1.0
Horizontal Position

Phase Shift
3.0
2.0
1.0
0.0

-1.0mm -0.5 0.0 0.5   1.0

600

400

200

0

with phase
correction

without
correction

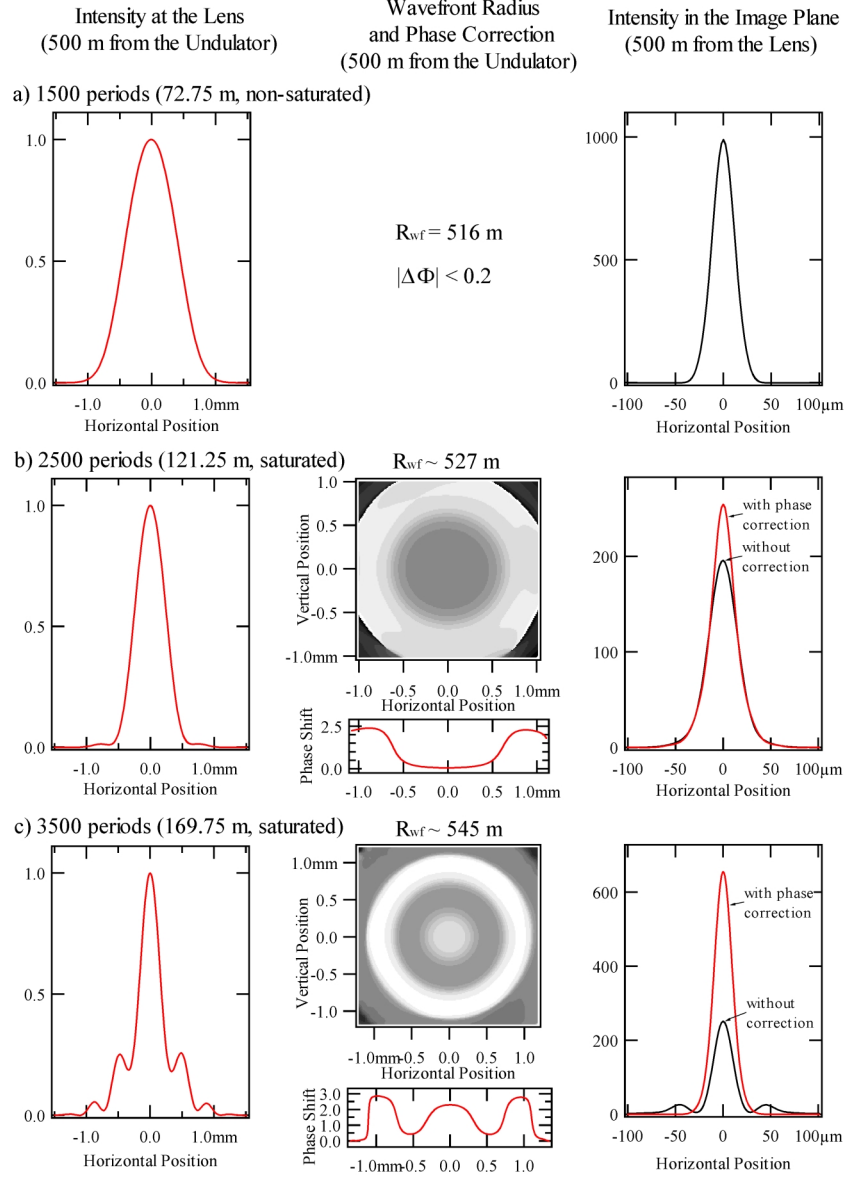-100 -50   0   50 100μm
Horizontal Position

Figure 9. Computed horizontal intensity profiles of SASE wavefronts at 500 m from the exit of undulator (left), approximate wavefront radii and phase corrections characterizing the phase difference of these wavefronts from that of the corresponding point sources (middle), and the intensity profiles in the image plane (right), for three different numbers of periods in the undulator: 1500 (a), 2500 (b), and 3500 (c).

4. CONCLUSIONS

The wave-optical calculations discussed in this paper enable a detailed analysis of the features of spontaneous and self-amplified spontaneous emission. This type of computation is important for third generation of SR sources and free-electron lasers, where the spatial coherence of the emitted radiation is very high over the large part of spectrum.

For most of the examples presented in this paper, the computation time was not larger than several minute on a 300 MHz PC. The high CPU-efficiency of these methods allows to apply them not only to the direct problems, but also to the inverse ones, like beamline optimization, beam diagnostics and experimental data processing.

5. ACKNOWLEDGEMENTS

6. REFERENCES

1. A.Hofmann and F.Meot, "Optical resolution of beam cross-section measurements by means of synchrotron radiation", *Nucl. Instrum. and Methods* **203**, pp.483-493, 1982.

2. K.-J.Kim, "Brightness, coherence and propagation characteristics of synchrotron radiation", *Nucl. Instrum. and Methods* **A246**, pp.71-76, 1986.

3. A.Ogata, "On optical resolution of beam size measurements by means of synchrotron radiation", *Nucl. Instrum. and Methods* **A301**, pp.596-598, 1991.

4. O.Chubar, "Resolution improvement in beam profile measurements with synchrotron light", *Proc. of IEEE Particle Accelerator Conference PAC-93*, vol.3, pp.2510-2512, 1993.

5. N.V.Smolyakov, "Wave-optical properties of synchrotron radiation", *Nucl. Instrum. and Methods* **A405**, pp.235-239, 1998.

6. R.Bosch, "Focusing of infra-red edge and synchrotron radiation", *Nucl. Instrum. and Methods* **A431**, pp.320-333, 1999.

7. O.Chubar, P.Elleaume and A.Snigirev, "Phase analysis and focusing of synchrotron radiation", *Nucl. Instrum. and Methods* **A435**, pp.495-508, 1999.

8. J.Bahrdt, "Wavefront propagation: design code for synchrotron radiation beamlines", *Applied Optics* **36** (19), pp.4367-4381, 1997.

9. O.Chubar, P.Elleaume, "Accurate and efficient computation of synchrotron radiation in the near field region", *Proc. of 6th European Particle Accelerator Conference EPAC-98*, pp.1177-1179, 1998.

10. O.Chubar, "Precise computation of electron beam radiation in non-uniform magnetic fields as a tool for the beam diagnostics", *Rev. Sci. Instrum.* **66**(2), pp.1872-1874, 1995.

11. J.D.Jackson, *Classical Electrodynamics*, 2nd. ed., New York: Wiley, 1975.

12. L.D.Landau, E.M.Lifshits, *The Classical Theory of Fields*, Pergamon, 1975.

13. G.A.Travish, "An overview of FEL simulation codes", X-ray Workshop, Gargnano, Italy, June 1997.

14. J.B.Murphy, C.Pellegrini, "Introduction to the physics of the free electron laser", *Laser Handbook*, edited by W.B.Colson, C.Pellegrini and A.Renieri, Elsevier Science Publisher B.V. **6**, pp.9-69, 1990.

15. W.B.Colson, "Classical free electron laser theory", *Laser Handbook*, edited by W.B.Colson, C.Pellegrini and A.Renieri, Elsevier Science Publisher B.V. **6**, pp.115-194, 1990.

16. M.Born, E.Wolf, *Principles of Optics*, 4th ed., Pergamon Press, 1970.

17. R.P.Walker, "Near-field effects in off-axis undulator radiation", *Nucl. Instrum. and Methods* **A267**, p.537, 1988.

18. Design of a 500 GeV e+e- Linear Collider with Integrated X-Ray Laser Facility, DESY Report 1997-048, Editors: R.Brinkmann, G.Materlik, J.Rossbach, A.Wagner.

19. S.Reiche, *Nucl. Instrum. and Methods* **A429**, pp.243-248, 1999; see also "Manual for GENESIS 1.3", available at "http://www.desy.de/~reichesv/genesis/genesis.html".

20. E.L.Saldin, E.A.Scheidmiller, M.V.Yurkov, *Physics Reports* **260**, pp.187-327, 1995.

21. P.Elleaume, J.Chavanne, B.Faatz, "Design considerations for a 1 Å SASE undulator", to appear in *Nucl. Instrum. and Methods*.